

Article

# Casimir Forces with Periodic Structures: Abrikosov Flux Lattices

Shunashi Guadalupe Castillo-López , Raúl Esquivel-Sirvent , Giuseppe Pirruccio  and Carlos Villarreal \* 

Instituto de Física, Universidad Nacional Autónoma de México, Apdo. Postal 20-364, Mexico City 01000, Mexico; shunashi@fisica.unam.mx (S.G.C.-L.); raul@fisica.unam.mx (R.E.-S.); pirruccio@fisica.unam.mx (G.P.)

\* Correspondence: carlos@fisica.unam.mx

**Abstract:** We investigate the influence of the Abrikosov vortex lattice on the Casimir force in a setup constituted by high-temperature superconductors subject to an external magnetic field. The Abrikosov lattice is a property of type II superconductors in which normal and superconducting carriers coexist and the latter define a periodic pattern with square symmetry. We find that the optical properties determined by spatial redistribution of the superconducting order parameter induce Casimir forces with a periodic structure whose minimal strengths coincide with the vortex cores.

**Keywords:** Casimir force; superconductor; quantum vortex; fluxon; Abrikosov lattice; vortex matter

## 1. Introduction

Seventy-five years have passed since, motivated by a suggestion by Niels Bohr during a walk, Hendrik Casimir proposed that vacuum fluctuations could induce an attractive force per unit area between two perfectly conducting parallel plates, a distance  $d$  apart, given by  $F = -\hbar c \pi^2 / 240 d^4$  [1] with  $\hbar = h/2\pi$  the reduced Planck constant and  $c$  the speed of light. A more realistic theory was proposed by Evgeny Lifshitz in 1956 by considering fluctuating electrodynamics, based on the fluctuation–dissipation mechanism. Lifshitz theory allows to determine the Casimir force in terms of the dispersive and dissipative properties of the materials [2], as described by its optical properties. Grounded on Lifshitz formulation, numerous experiments [3–13] have been performed on measuring the Casimir forces involving a diversity of experimental arrangements and materials [14,15]. The influence and taming of these forces in the design and construction of micro- and nanodevices is a current field of research. Extensive treatments of the Casimir effect and its applications, are presented in Refs. [16–20].

In spite of the fruitful advances in the investigations of the Casimir effect there exist yet pending fundamental problems on the basic theory, concerning the role of dissipative mechanisms on the strength of the force between metallic bodies. These may involve electron scattering by impurities, other electrons, phonons, etc., yielding a total scattering rate  $\tau^{-1} = \tau_{\text{el-imp}}^{-1} + \tau_{\text{el-el}}^{-1}(T) + \tau_{\text{el-ph}}^{-1}(T) + \dots$ . Actually, the inclusion of this kind of contributions in the theoretical characterization of the optical response of materials involved in a given setup should be necessary to achieve congruence with the fluctuation–dissipation theorem underlying the Lifshitz theory. However, earlier measurements of Casimir forces in metals at room temperature at body separations  $d \approx 50\text{--}600$  nm showed consistence with theoretical predictions if dissipative effects are neglected. This hypothesis is also consistent with more recent experimental studies of the gradient of the Casimir force between metallic surfaces performed at larger separations,  $d > 700$  nm, such that  $k_B T \sim \hbar c/d$  [21–23], with  $k_B$  the Boltzmann constant. On the contrary, experiments carried out at micrometer distances to measure the total magnitude of the Casimir force display a better agreement with predictions including electronic relaxation [19]. The main difference between the results at small and large separations, is that in the latter thermal effects become important.

It has been proposed that the study of the Casimir effect in superconducting (SC) materials may constitute an excellent scenario to assess the influence of relaxation phenomena



Citation: Castillo-López, S.G.; Esquivel-Sirvent, R.; Pirruccio, G.; Villarreal, C. Casimir Forces with Periodic Structures: Abrikosov Flux Lattices. *Physics* **2024**, *6*, 394–406. <https://doi.org/10.3390/physics6010026>

Received: 4 December 2023

Revised: 27 January 2024

Accepted: 30 January 2024

Published: 12 March 2024



**Copyright:** © 2024 by the authors. Licensee MDPI, Basel, Switzerland. This article is an open access article distributed under the terms and conditions of the Creative Commons Attribution (CC BY) license (<https://creativecommons.org/licenses/by/4.0/>).

on the strength of the Casimir force between metallic bodies [24–28]. This is motivated by the finding that charge carriers in these materials exhibit a transition from dissipative transport to a dissipationless coherent behavior at a critical temperature  $T = T_c$ . However, measurements of the influence of the SC transition on the Casimir force in setups involving conventional BCS (Bardeen–Cooper–Schrieffer) superconductors turn out to be extremely difficult, since for typical values  $T_c \sim 1$  K, and  $k_B T_c \ll \hbar c/d$  for sub- $\mu\text{m}$  body separations. Therefore, indirect approaches have been proposed based on observations of the Casimir-induced shift of the critical magnetic field  $H_c$  of a thin superconducting film, or differential measurements of the Casimir force [29,30].

This suggests that the use of high-temperature superconductors (HTSCs), with  $T_c \approx 100$  K, could constitute a suitable alternative to perform a direct analysis of the effect of the SC transition on the Casimir effect. In previous studies, we investigated the Casimir forces between objects made of optimally doped  $\text{YBa}_2\text{Cu}_3\text{O}_{7-\delta}$  (YBCO), with  $T_c = 93$  K, either in thermal [31], or out of thermal equilibrium [32]. In the first case, we found that the Casimir force displays an abrupt increment as  $T$  approaches  $T_c$  from above,  $T \rightarrow T_c$ . On the other hand, for  $T < T_c$ , the (force  $\times$  distance) approaches a constant in the limit  $T \ll T_c$ . In the second case, each slab was in local equilibrium with a thermal reservoir at respective temperatures,  $T_1 = 300$  K and  $T_2$ , where  $300 \geq T_2 \geq 0$  K. In contrast with the thermal equilibrium situation, the Casimir force displays an abrupt decrement in the transit from normal metal to the SC state as  $T_2 \rightarrow T_c$ . The low-temperature asymptotic behavior of the force is similar to that displayed in the equilibrium situation.

To get further insight on the influence of superconductivity-related effects on the Casimir effect, in this paper, we study the effect of the Abrikosov lattice (AL) [33] on the local properties of Casimir forces associated to high-temperature superconductors (HTSCs). The AL is a manifestation of the Meissner effect, in which the presence of an external magnetic field induces surface screening supercurrents, which expel out the magnetic field lines from the material's interior within a London penetration length  $\lambda_L(T) \sim n_s(T)^{-1/2}$ . Here,  $n_s(T)$  is the number density of Cooper pairs (CPs) at a temperature  $T$ . In the case of type-II superconductors, such as YBCO, the Meissner effect involves the existence of a mixed phase of coexistence of normal and SC charge carriers determined by two critical magnetic fields,  $H_{c1} < H_{c2}$ . For values of the applied field higher than  $H_{c1}$ , magnetic flux lines penetrate the sample in the form of quantum vortices,  $\Phi_0 = h/2e$ , with  $e$  the elementary charge, thus inducing local screening currents to overcome the applied field [34]. Upon increasing magnitude of the field, the vortex density increases and saturates at the upper critical field  $H_{c2}$ , where superconductivity disappears. Remarkably, as shown by Alexei Abrikosov [33], for intensities of the applied field just below  $H_{c2}$  the vortices align in a compact square lattice with period  $L_x = L_y = \sqrt{2\pi}\xi(T)$ , where  $\xi(T)$  is the CP coherence length. In the case of YBCO,  $\xi(0) \equiv \xi_0 \approx 1.65$  nm, and  $\lambda_L(0) \equiv \lambda_0 \approx 156$  nm, while the temperature-independent ratio  $\kappa = \lambda_L(T)/\xi(T) \approx 95$  [34].

It can be shown that the AL vortices strongly repel each other, giving rise to highly correlated configurations which are stable when thermal fluctuations and disorder are both negligible. A measure of the magnitude of the energy associated to thermal fluctuations with respect to the magnetic condensation energy is provided by the Ginzburg number [35],  $G_i = 2\gamma^2\kappa^4(k_B T_c/H_{c2}(0))^2\xi_0^3$ , where  $\gamma$  is a measure of the anisotropic conductivity (discussed below). In the case of conventional BCS superconductors,  $G_i = 10^{-7}$ . In comparison, in the case of HTSCs,  $T_c \sim 10^2$  K and  $\kappa \sim 10^2$ , implying that  $G_i \sim 10^{-2}$ . This relatively large value of  $G_i$  joined with the feature that these materials display a layered anisotropic structure at the atomic level, leads to the manifestation of a manifold of phenomena generally termed as vortex matter, encompassing a complex phase diagram under different environmental conditions and material compositions [36]. Thus, thermal fluctuations may significantly alter the properties of the AL, generally leading to melting towards a liquid phase displaying vortex deformation, entanglement or migration. Superposed with repulsive interactions and thermal fluctuations, disorder due to material imperfections induce vortex pinning, which may conduce to the formation of glassy configurations [35–37].

Vortex matter has been investigated by recurring to techniques such as scanning tunneling microscopy [38] or muon spin rotation [39]. In addition, the possibility of using cold atoms to assess vortex-noise has been considered in the literature [40].

In order to examine the influence of the AL on the Casimir force, in this study we consider a setup, depicted in Figure 1, constituted by a spherical Au nanoparticle located at a minimum distance  $d$  from a planar YBCO substrate, in presence of an applied magnetic field directed along the  $z$ -axis. We show that the force acquires a spatial structure congruent with the AL due to the modulation imparted by the vortices on the dielectric permittivity.

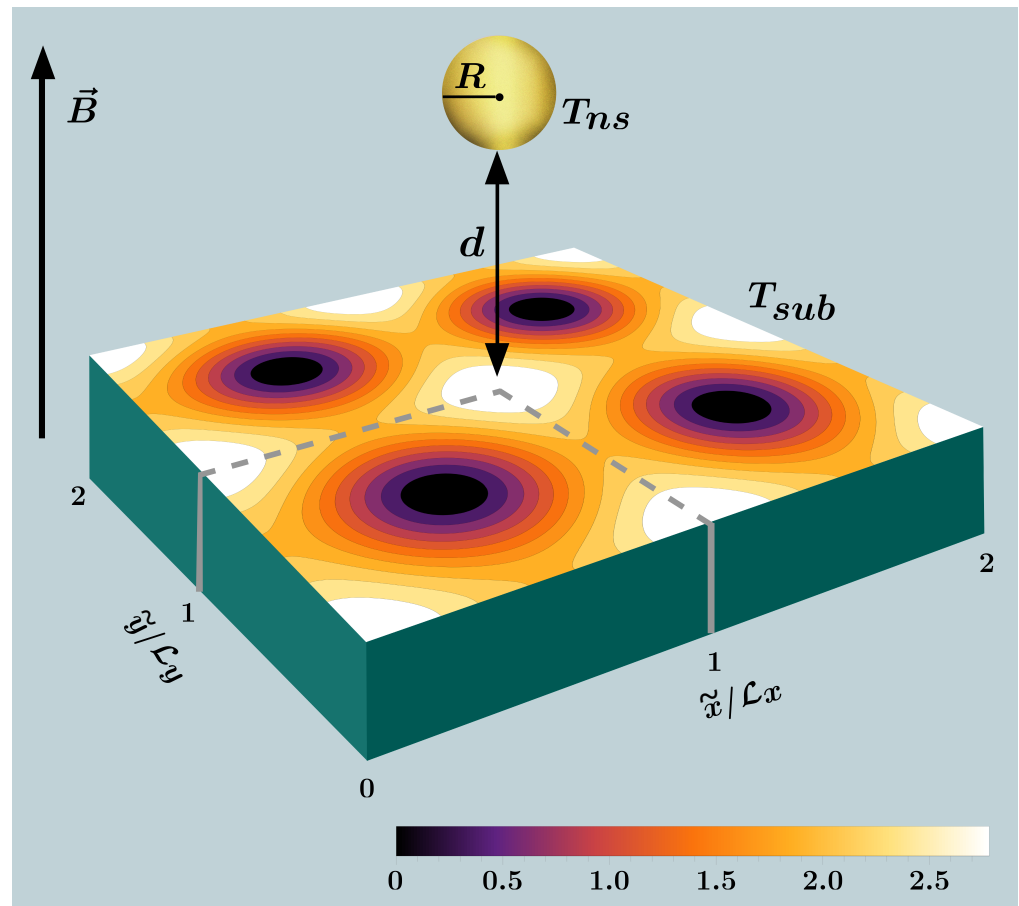


**Figure 1.** Setup consisting of a spherical Au nanoparticle of radius  $R$  located at a minimum distance  $d$  from a planar substrate made of optimally-doped YBCO ( $\text{YBa}_2\text{Cu}_3\text{O}_{7-\delta}$ ), both at the same temperature  $T = T_{ns}$  and  $T_{sub}$ , respectively,—in presence of an applied magnetic field directed along the  $z$  axis. We show the resulting lattice structure with elementary cells of nondimensional spatial periods  $a = \mathcal{L}_x = \mathcal{L}_y$ . Induced supercurrents coincide with equiprobability contours defined by the number density of Cooper pairs,  $n_s = |\Psi(\vec{r})|^2$ , where  $\Psi(\vec{r})$  is the superconducting order parameter. The vortex cores of radius  $\zeta$  correspond to the darkest inner zones.  $\vec{B}$  denotes the magnetic field, and the tilde stands for adimensional variables,  $\tilde{x} = x/\lambda_{ab}$  and  $\tilde{y} = y/\lambda_{ab}$ , where  $\lambda_{ab}$  represents the  $ab$ -plane penetration length.

In what follows, we present the formalism aimed to evaluate the Casimir force between a planar substrate and a nanosphere, which relies upon the frequency-dependent optical properties of the involved materials. To investigate the optical response of YBCO under the action of an external magnetic field, we then discuss a generalization of the Ginzburg–Landau (GL) theory of superconductivity, which allows the consideration of the anisotropic properties HTSCs, allowing the characterization of the number density of SC pairs,  $n_s(\mathbf{r})$ , with a spatial dependence induced by the action of the applied magnetic field, as provided by the Abrikosov solution of the GL equation. We then discuss the thermal behavior of

$n_s(\mathbf{r})$  by taking into account that SC charge carriers in HTSCs may be described as a 2D (2-dimensional) gas of weakly-interacting CPs able to form a Bose–Einstein condensate (BEC). In Section 2, we model the optical response of YBCO by combining the derived expression for  $n_s(\mathbf{r}, T)$  with experimental data for the YBCO dielectric function obtained in the normal ( $T = 100$  K) and SC regime ( $T = 2$  K). We then integrate the former antecedents to evaluate the Casimir force associated to the AL, and discuss the derived results.

## 2. Theory and Definitions

### 2.1. Casimir Force between a Nanosphere and a Planar Substrate

The theory of the Casimir effect between a sphere and a planar surface beyond the Proximity Force Approximation has been investigated within alternative perspectives, including some developed by authors of the present study [18,41–47]. In this Section, we extend the formalism previously presented in Refs. [41–43] to calculate the finite-temperature Casimir force for the nanosphere-substrate setup displayed in Figure 1, with the corresponding dielectric function of the nanosphere,  $\epsilon_{ns}(\omega)$ , and substrate,  $\epsilon_{sub}(\mathbf{r}, \omega)$ . We first evaluate the zero-temperature interaction energy as a sum over proper frequencies,  $\omega_k(\mathbf{r}_\perp; d)$ , of the considered configuration:

$$\mathcal{E}(\mathbf{r}_\perp; d) = \frac{1}{2} \sum_k (\hbar\omega_k(\mathbf{r}_\perp; d) - \hbar\omega_k(\mathbf{r}_\perp; d \rightarrow \infty)), \quad (1)$$

where  $\mathbf{r}_\perp(x, y)$ . Straightforward use of the argument principle method lets us express the sum over proper mode frequencies as a sum over the zeros of a spectral function  $G(\omega; \mathbf{r}_\perp; d)$  (discussed below). This is determined by the solutions of Maxwell equations with boundary conditions satisfied by the plate-sphere setup:

$$\mathcal{E}(\mathbf{r}_\perp; d) = \frac{1}{2\pi i} \oint_C \frac{\hbar\omega}{2} \frac{\partial}{\partial\omega} [\log G(\omega; \mathbf{r}_\perp, d) - \log G(\omega; \mathbf{r}_\perp, d \rightarrow \infty)] d\omega. \quad (2)$$

Here, the (counter clock-wise) contour  $\mathcal{C}$  is defined along the imaginary axis of the complex  $\omega$ -plane and a semicircle in the right hand of this plane with its radius tending to infinity. The integral along the semicircle yields a null contribution, and the integral in Equation (3) may be evaluated by considering a contour between  $-i\infty$  and  $i\infty$ . An integration by parts leads to

$$\mathcal{E}(\mathbf{r}_\perp; d) = -\frac{\hbar}{4\pi} \int_{-\infty}^{\infty} [\log G(\omega; \mathbf{r}_\perp, d) - \log G(i\zeta; \mathbf{r}_\perp, \infty)] d\zeta. \quad (3)$$

The Casimir force is then obtained by calculating the derivative  $F(\mathbf{r}_\perp; d) = -\partial\mathcal{E}(\mathbf{r}_\perp; d)/\partial d$ . The eigenfrequency set of the sphere-substrate setup  $\{\omega_k(\mathbf{r}_\perp; d)\}$  is obtained by assuming that the vacuum fluctuations induce a charge distribution on the sphere, described at lowest level, as a point dipole moment located at its center:

$$\mathbf{p}_{ns}^0(\omega) = \alpha(\omega) \mathbf{E}^{vac}(\omega), \quad (4)$$

where  $\alpha(\omega) = 4\pi R^3(\epsilon_{ns} - 1)/(\epsilon_{ns} + 2)$  denotes the nanosphere polarizability with  $R$  the nanosphere radius and  $\mathbf{E}^{vac}$  denoting the electric field in vacuum. This dipole moment introduces in turn a charge distribution in the YBCO half-space. By using the images method it follows that the total induced dipole moment on the sphere is

$$\mathbf{p}_{ns}(\omega; \mathbf{r}_\perp) = \alpha(\omega) [\mathbf{E}^{vac}(\omega) + \mathbb{T} \cdot \mathbf{p}_{sub}(\mathbf{r}_\perp)]. \quad (5)$$

Here,  $\mathbb{T}$  is the dipole-dipole interaction tensor  $\mathbb{T} = (3\mathbf{r}_0\mathbf{r}_0 - r_0^2\mathbb{I})/r_0^5$ , with  $\mathbf{r}_0$  a vector joining the center of the sphere and its image dipole below the substrate surface. In turn, the relation between the dipole moment on the sphere and the dipole moment induced on the YBCO substrate is  $\mathbf{p}_{sub}(\omega; \mathbf{r}_\perp) = f_c(\omega; \mathbf{r}_\perp) \mathbb{M} \cdot \mathbf{p}_{ns}(\mathbf{r}_\perp)$ , where  $\mathbb{M} = \text{diag}(-1, -1, 1)$  is

a diagonal matrix in the chosen coordinate frame, and the contrast factor  $f_c(\omega; \mathbf{r}_\perp) \equiv (1 - \epsilon_{\text{sub}}(\omega; \mathbf{r}_\perp)) / (1 + \epsilon_{\text{sub}}(\omega; \mathbf{r}_\perp))$ . By substituting  $\mathbf{p}_{\text{sub}}(\omega; \mathbf{r}_\perp)$  into Equation (5), one obtains:

$$\left[ \alpha^{-1}(\omega)\mathbb{I} + f_c(\omega; \mathbf{r}_\perp)\mathbb{M} \cdot \mathbb{T} \right] \cdot \mathbf{p}_{\text{ns}}(\omega; \mathbf{r}_\perp) = \mathbf{E}^{\text{vac}}(\omega), \tag{6}$$

which, by introducing the function  $u(\omega) = [1 - \epsilon_{\text{ns}}(\omega)]^{-1}$  and explicitly substituting  $\alpha(\omega)$ , may be re-expressed as the secular equation:

$$[-u(\omega)\mathbb{I} + \mathbb{H}(\mathbf{r}_\perp)] \cdot \mathbf{p}_{\text{ns}}(\omega; \mathbf{r}_\perp) = \tilde{\mathbf{E}}^{\text{vac}}(\omega), \tag{7}$$

where  $\mathbb{H}(\mathbf{r}_\perp) = (1/3)[\mathbb{I} + R^3 f_c(\omega; \mathbf{r}_\perp)\mathbb{M} \cdot \mathbb{T}]$ , and  $\tilde{\mathbf{E}}^{\text{vac}} = (1/3)R^3 \mathbf{E}^{\text{vac}}$ . By performing the change of variable  $\omega \rightarrow i\zeta$ , it follows that the matrix  $\mathbb{H}$  in Equation (7) is real. This allows us to introduce the spectral function such that

$$G(i\zeta; \mathbf{r}_\perp, d) \equiv \prod_l [-u(i\zeta) + \eta_l(i\zeta; \mathbf{r}_\perp, d)] = 0, \tag{8}$$

which in the present case implies three eigenvalues,

$$\eta_{1,2}(i\zeta; \mathbf{r}_\perp, d) = \frac{1}{3} \left[ 1 + \frac{f_c(i\zeta; \mathbf{r}_\perp)}{[2(1 + d/R)]^3} \right]; \quad \eta_3(i\zeta; \mathbf{r}_\perp, d) = \frac{1}{3} \left[ 1 + \frac{2f_c(i\zeta; \mathbf{r}_\perp)}{[2(1 + d/R)]^3} \right], \tag{9}$$

whose structure reflects the dipole–dipole interaction described by the tensor  $\mathbb{T}$ , and  $\eta_{1,2}$  correspond to dipoles parallel to the surface, while  $\eta_3$  is perpendicular. Substitution of  $G(i\zeta; \mathbf{r}_\perp, d)$  into Equation (2) leads to a final expression for Casimir force at null temperature:

$$\begin{aligned} F(\mathbf{r}_\perp, d) &= \frac{\hbar}{4\pi} \frac{\partial}{\partial d} \sum_l \int_{-\infty}^{\infty} \log[-u(i\zeta) + \eta_l(i\zeta; \mathbf{r}_\perp, d)] d\zeta \\ &= \frac{\hbar}{16\pi R} \frac{1}{(1 + d/R)^4} \int_{-\infty}^{\infty} \left[ \frac{f_c(i\zeta; \mathbf{r}_\perp)}{-u(i\zeta) + \eta_1(i\zeta; \mathbf{r}_\perp, d)} + \frac{f_c(i\zeta; \mathbf{r}_\perp)}{-u(i\zeta) + \eta_3(i\zeta; \mathbf{r}_\perp, d)} \right] d\zeta, \end{aligned} \tag{10}$$

where the feature that  $\eta_1(i\zeta; \mathbf{r}_\perp, d) = \eta_2(i\zeta; \mathbf{r}_\perp, d)$  has been considered.

This result may be generalized to the finite-temperature regime by use of the Matsubara formalism. In this approach, the frequency integration is replaced by a summation over discrete frequencies  $\zeta_n = 2\pi k_B T n / \hbar$ , with  $n$  an integer number. In that case, the final expression for temperature-dependent Casimir force is:

$$F(\mathbf{r}_\perp, d; T) = \frac{k_B T}{4R} \frac{1}{(1 + d/R)^4} \sum_{n=0}' \left[ \frac{f_c(i\zeta_n; \mathbf{r}_\perp)}{-u(i\zeta_n) + \eta_1(i\zeta_n; \mathbf{r}_\perp)} + \frac{f_c(i\zeta_n; \mathbf{r}_\perp)}{-u(i\zeta_n) + \eta_3(i\zeta_n; \mathbf{r}_\perp)} \right], \tag{11}$$

where the prime implies that the  $n = 0$  term should be multiplied by a factor 1/2.

The influence of higher-order multipoles on the Casimir force for the present configuration has been studied in Refs. [42,43]. It follows that for sphere–substrate multipolar interaction of order  $l$  and  $l'$ , respectively, the interaction energy  $\mathcal{E}(\mathbf{r}_\perp; d) \sim f(\mathbf{r}_\perp) / (2[R + d])^{l+l'+1}$ , and therefore,  $F(\mathbf{r}_\perp; d) \sim f(\mathbf{r}_\perp) / (2[R + d])^{l+l'+2}$ . However, specific calculations [42] indicate that the contributions for  $l, l' > 1$ , only become relevant for distances  $d/R < 2$ , consistently with the dipolar approximation considered in this study.

### 2.2. Ginzburg–Landau Theory and the Optical Response of the YBCO Substrate

In the expressions derived in Section 2.1, the functions  $u(\omega)$  and  $f_c(\omega)$  are respectively determined by the dielectric response of the nanosphere,  $\epsilon_{\text{ns}}$ , and the planar substrate,  $\epsilon_{\text{sub}}$ . The dielectric properties of the gold nanosphere may be straightforwardly represented by a Drude function  $\epsilon_{\text{ns}}(\omega) = 1 - \omega_{\text{Au}}^2 / (\omega^2 + i\gamma_{\text{Au}}\omega)$ , where the gold plasma frequency,  $\omega_{\text{Au}} = 9.1$  eV, and the inverse scattering rate,  $\gamma_{\text{Au}} = 0.02$  eV. Therefore,  $u(i\zeta) = -(\zeta^2 + \gamma_{\text{Au}}\zeta) / \omega_{\text{Au}}^2$ .

On the other hand, to characterize the dielectric response of the YBCO subject to the action of an applied magnetic field,  $\mathbf{H}$ , we put forth a straightforward variation of the GL theory of superconductivity that takes into account specific SC features of HTSCs, such as YBCO. In the GL theory, the transit to the SC state is described as a second-order phase transition determined by a complex order parameter,  $\Psi(\mathbf{r})$ , null in the normal phase, but finite in the SC phase, characterizing a long-range order specified by the number density of SC pairs,  $n_s(\mathbf{r}) = |\Psi(\mathbf{r})|^2$ . We incorporate in the GL formalism the following findings [48]: (i) cuprate superconductors exhibit a layered crystallographic structure in which superfluid transport of CPs occurs mainly along  $\text{CuO}_2$  planes (the  $ab$ -planes), whereas CP transport along the perpendicular  $c$ -axis occurs due to Josephson tunneling, with respective effective masses,  $m_{ab}^*$  and  $m_c^*$ , reflecting an anisotropic charge transport measured by the ratio  $\gamma^2 = m_c^*/m_{ab}^* \approx 50$ , (ii) an extremely short CP coherence length, such that the GL parameter  $\kappa \gg 1$ . The finding that  $\gamma^2 \gg 1$  implies that YBCO is an uniaxial material with a concomitant anisotropic dielectric response characterized by the diagonal tensor  $\epsilon = \text{diag}(\epsilon_{ab}, \epsilon_{ab}, \epsilon_c)$  in the coordinate system depicted in Figure 1. However, a related study on the radiative heat transfer between nearby YBCO surfaces [49] revealed that electromagnetic mode contributions involving  $\epsilon_c$  are relevant only for thin film configurations. Therefore, in the following, we assume that  $\epsilon_{\text{sub}} = \epsilon_{ab}$ . On the other hand, the joint conditions (i) and (ii) are indicative of a strongly binding pair interaction, leading the formation of a 2D gas of weakly-interacting particles, able to form a BEC [50].

In this framework, the anisotropic free energy density in the SC state in presence of a magnetic field  $\mathbf{B}(\mathbf{r}) = \nabla \times \mathbf{A}(\mathbf{r})$ , with  $\mathbf{A}$  the electromagnetic potential, can be expressed as

$$f_s(T) = f_n(T) + \frac{1}{2}(\hat{\pi}\Psi)^\dagger \cdot \left(\frac{1}{m^*}\right) \cdot (\hat{\pi}\Psi) + a_T|\Psi|^2 + \frac{b}{2}|\Psi|^4 + \frac{1}{2\mu_0}\mathbf{B}^2(\mathbf{r}), \quad (12)$$

where  $f_n(T)$  is the normal state contribution,  $\Psi$  is the superconducting order parameter, the symbol  $^\dagger$  denotes hermitian conjugate,  $\mu_0$  is magnetic permeability of free space, the canonical momentum  $\hat{\pi} = -i\hbar\nabla + e^*\mathbf{A}$ , with  $e^* = 2e$  the CP charge, and the reciprocal mass tensor is also diagonal in the chosen coordinate system:  $(1/m^*) = \text{diag}(1/m_{ab}^*, 1/m_{ab}^*, 1/m_c^*)$ . In the original GL approach,  $a_T = a_0(T - T_c)$  and  $b > 0$ ; however, as shown in Section 2.3, a more accurate description of the physical properties of SC materials can be achieved by considering alternative temperature parameterizations.

In the SC state, the total energy is obtained by spatial integration of Equation (12),  $F_s = \int f_s(T)d^3r$ . It follows that the functional differentiation,  $\delta F_s(T)/\delta\Psi^*(\mathbf{r})$ , then leads to the anisotropic GL equation

$$-\frac{\hbar^2}{2}\left[\nabla - \frac{ie^*}{\hbar}\mathbf{A}\right] \cdot \left(\frac{1}{m^*}\right) \cdot \left[\nabla - \frac{ie^*}{\hbar}\mathbf{A}\right]\Psi + (a_T + b|\Psi|^2)\Psi = 0, \quad (13)$$

while the differentiation  $\delta F_s(T)/\delta\mathbf{A}(\mathbf{r})$  yields the current density

$$\mathbf{J}_s = -\frac{i\hbar e^*}{2}\left(\frac{1}{m^*}\right) \cdot [\Psi^*\nabla\Psi - \Psi\nabla\Psi^*] - \left(\frac{1}{m^*}\right) \cdot e^{*2}\mathbf{A}|\Psi|^2. \quad (14)$$

It can be shown that the mass anisotropy induces in turn anisotropic coherence lengths,  $\xi_j(T)$ , satisfying the relations  $\xi_{ab}^2(T) = \hbar^2/2m_{ab}^*|a_T|$ , and  $\xi_c^2(T) = \hbar^2/2m_c^*|a_T|$  [48]. In absence of external fields or material boundaries, the former equations predict a second-order phase transition, with an order parameter magnitude,  $|\Psi_\infty|^2 = 0$ , for  $a_T > 0$ , and  $n_s = |\Psi_\infty|^2 = -a_T/b$ , for  $a_T < 0$ , and a null current density. In this case, the condensation energy of the superconductor (per unit volume) is given by [48]

$$f_s(T) - f_n(T) = -a_T^2/2b = -\mu_0 H_{c2}^2(T)/4\kappa^2, \quad (15)$$

with  $H_{c2}(T) = \Phi_0/2\pi\xi_{ab}^2(T)$ . In the general case, Equations (13) and (14) represent a coupled equation system; however, for type II materials this system uncouples by taking

into account that a thermodynamic phase transition also occurs for magnetic fields  $H = H_{c2}$ . Since the phase transition is of second order,  $\Psi$  is small and so is the magnetization  $\mathbf{M}$ . Therefore,  $\mathbf{B} = \mu_0(\mathbf{H} + \mathbf{M}) \approx \mu_0\mathbf{H}$ , where  $\mathbf{H}$  is the applied field. This implies that, near  $H_{c2}$ , the spatial variation in  $\mathbf{B}(\mathbf{r})$  can be neglected and consider that it has the form  $\mathbf{B} = B \mathbf{e}_z$ , where  $\mathbf{e}_z$  is directed along the crystallographic  $c$ -axis. Then, in the Landau gauge, the vector potential  $\mathbf{A} = Bx \mathbf{e}_y$ . A further consequence of the smallness of  $\Psi$  is that the GL equation may be linearized by dropping cubic term in Equation (13). Then, the GL equation becomes

$$\frac{-\hbar^2}{2m_{ab}^*} \left( \nabla_{\perp} - \frac{ie^*}{\hbar} B x \mathbf{e}_y \right)^2 \Psi - \frac{\hbar^2}{2m_c^*} \frac{\partial^2}{\partial z^2} \Psi = |a_T| \Psi. \tag{16}$$

As shown by Abrikosov [33], Equation (16) admits Landau-level solutions of the form  $\Psi(\mathbf{r}) = \Phi(\mathbf{r}_{\perp}) e^{ik_z z}$ , where the ground state is given by  $k_z = 0$ , and

$$\Phi(\mathbf{r}_{\perp}) = \sum_{n=-\infty}^{\infty} C_n e^{i(2\pi n y)/L_y} \exp[-(x + n\Phi_0/BL_y)^2 / \xi_{ab}^2(T)], \tag{17}$$

which is a periodic function provided  $C_n = C_{n+\nu}$ , for some integer  $\nu$ . The case  $\nu = 1$  corresponds to a square lattice as displayed by HTSCs, while the case  $\nu = 2$  yields a triangular lattice, characteristic of conventional superconductors [34]. The stability of these solutions can be analyzed by incorporating the effects of nonlinear terms in the description. This is determined by the Abrikosov parameter,  $\beta_A = \langle |\Psi|^4 \rangle / \langle |\Psi|^2 \rangle^2$ . In the homogeneous case,  $\beta_A = 1$ , whereas  $\beta_A > 1$  implies less favorable energies. In particular, the energy of the triangular configuration is smaller than that of the square one by less than 1% [34]. In the square lattice configuration, the summation may be re-expressed in terms of a Jacobi theta function,  $\theta_3(z; q) = \sum_{n=-\infty}^{\infty} q^{n^2} e^{2inz}$ , so that

$$\Phi(\tilde{x}, \tilde{y}) = C e^{-\frac{1}{2}\kappa^2 \tilde{x}^2} \theta_3 \left[ 1; \sqrt{2\pi} \kappa i(\tilde{x} + i\tilde{y}) \right]. \tag{18}$$

In this case,  $\kappa = \lambda_{ab} / \xi_{ab}$  where  $\lambda_{ab}$  is the  $ab$ -plane penetration length, while  $\tilde{x} = x / \lambda_{ab}$ ,  $\tilde{y} = y / \lambda_{ab}$ . Notice that  $\lambda_{ab}$  describes the magnetic field screening by supercurrents flowing along the  $ab$ -plane. Figure 1 depicts the resulting contours of constant probability defined by  $|\Phi(\tilde{\mathbf{r}}_{\perp})|^2$ . We observe a lattice structure with square elementary cells with dimensionless periods  $\mathcal{L}_x = \mathcal{L}_y = \sqrt{2\pi} / \kappa$ . By writing  $\Phi(\tilde{\mathbf{r}}_{\perp}) = |\Phi(\tilde{\mathbf{r}}_{\perp})| e^{i\chi(\tilde{\mathbf{r}}_{\perp})}$  it follows that the GL current density is given by  $\mathbf{J}_s = (\hbar e^* / 2m_{ab}^*) |\Phi|^2 (\nabla \chi - (e^* / \hbar) \mathbf{A})$ , indicating that supercurrent lines coincide with the equi-probability contours, being the vortex cores located at the darkest zones of the figure. Notice that the vortex size can be tuned by the substrate temperature  $T$ , which modulates the lattice parameter. In normal units, it follows that  $L_x(T) = L_y(T) = \sqrt{2\pi} \xi_{ab}(T)$ , so that  $L_x(2\text{K}) \approx 4 \text{ nm}$ , whereas  $L_x(90\text{K}) \approx 16 \text{ nm}$ .

### 2.3. Thermal Properties of the Order Parameter

We describe the thermal properties of the order parameter by recurring to the London two-fluid model of superconductivity, inspired in turn by the two-fluid model of the superfluid He<sup>4</sup>. This model assumes that the charge density,  $n$ , at a fixed position, is split as a sum of normal and SC contributions,  $n = n_n(T) + n_s(T)$ . The temperature behavior of  $n_s(T)$  is frequently described according to the Casimir–Gorter model,  $n_s(T)/n = 1 - (T/T_c)^4$  [51]. However, this empirical relation is in clear disagreement with experimental observations [48].

We consider instead, as mentioned above, that CPs define a 2D gas of weakly-interacting particles with BE statistical properties. As a consequence, the energy excitation spectrum is given by Bogoliubov expression  $E_k = [(\hbar c_s k)^2 + (\hbar^2 k^2 / 2m^*)^2]^{1/2}$  which, in the low-momentum limit, leads to a phonon dispersion relation,  $E_k \approx \hbar c_s k$ , with  $c_s$  the sound’s speed, consistent with Landau’s criterion for superfluid particle transport [52]. In

that case, we assume the pair occupancy density at any given position can be expressed, for  $T < T_{\text{BEC}}$ , in the form [53]

$$n^{2D} = n_0^{2D}(T) + \sum_{\mathbf{k} \neq 0} \frac{1}{\exp(\hbar c_s k / k_B T) - 1}. \tag{19}$$

Here,  $T_{\text{BEC}} = \left(2\pi\hbar^2 c_s^2 n^{2D} / k_B^2 \zeta(2)\right)^{1/2}$ , and  $\zeta(2)$  is a Riemann’s zeta function. The summation in Equation (19) can be straightforwardly evaluated by integrating over a 2D density of states. It follows that  $n_0^{2D}(T) / n^{2D} = 1 - (T/T_c)^2$  [53,54]. Taking into account that in the dilute regime the condensate and the density of superfluid charge carriers coincide, we identify  $T_{\text{BEC}} = T_c$ . This latter result implies, in particular, that the penetration length satisfies the universal relation  $\lambda_{ab}^2(0) / \lambda_{ab}^2(T) = 1 - (T/T_c)^2$ , which has shown to represent an accurate description of experimental data for YBCO systems under an ample range of doping levels in the whole temperature interval  $0 < T < T_c$  [54–56]. By assuming now that the former results hold at every position over the SC substrate,  $n_0^{2D}(\mathbf{r}, T) \approx n_s^{2D}(\mathbf{r}, T)$ , and then

$$n_s^{2D}(\mathbf{r}_\perp, T) = |\Phi(\mathbf{r}_\perp)|^2 \left[1 - (T/T_c)^2\right]. \tag{20}$$

#### 2.4. YBCO Dielectric Response

The optical properties of HTSCs have been experimentally investigated for different compounds at several temperatures and frequencies using reflectivity and impedance-type measurements [57–59]. In particular, the dielectric function,  $\epsilon(\omega)$ , of YBCO samples has been measured in the normal and SC states at  $T = 100$  K and  $T = 2$  K, respectively. Notably, the estimated values of the optical parameters remain practically unaltered in these temperature extremes. In particular, the plasma frequency,  $\omega_p^2 = e^{*2}n / \epsilon_0 m^*$ , satisfies  $\omega_p(2\text{K}) = \omega_p(100\text{K}) = 0.75$  eV, suggesting that London’s two-fluid model of superconductivity can be employed to derive an interpolation,  $\epsilon(\omega; T)$ , valid in the entire temperature range  $2 < T < 100$  K. For  $T > T_c$ , an accurate representation of the dielectric response includes a constant term,  $\epsilon_\infty$ , in the optical spectrum, as well as Drude, mid-infrared (MIR), and  $N_{\text{ph}}$  phonon contributions:

$$\epsilon_{ab}^{(n)}(\omega) = \epsilon_\infty - \frac{\omega_p^2}{\omega^2 + i\gamma(T)\omega} - \frac{\Omega_{\text{MIR}}^2}{\omega^2 - \omega_{\text{MIR}}^2 + i\Gamma_{\text{MIR}}\omega} - \sum_{r=1}^{N_{\text{ph}}} \frac{\Omega_{\text{ph}}^2}{\omega^2 - \omega_r^2 + i\gamma_r\omega}. \tag{21}$$

Here,  $\epsilon_\infty = 3.8$ , the inverse scattering rate  $\gamma(T) = 0.037 + \gamma_1 T$  eV, with  $\gamma_1 = 8 \times 10^{-15}$  eV/K, and the MIR parameters  $\Omega_{\text{MIR}} = 2.6$  eV,  $\omega_{\text{MIR}} = 0.26$  eV,  $\Gamma_{\text{MIR}} = 1$  eV, whereas the phonon parameters are given in Refs. [57,58]. In the SC regime, dissipative scattering does not occur, so that  $\gamma \rightarrow 0$ . In that limit,  $(\omega \pm i\gamma)^{-1} \rightarrow \mathcal{P}(1/\omega) \mp i\pi\delta(\omega)$ , with  $\delta(\omega)$  the Dirac delta function, and the dielectric function becomes:

$$\begin{aligned} \epsilon_{ab}^{(s)}(\omega; \mathbf{r}_\perp) = \epsilon_\infty & - \left[ \frac{i\pi\omega_p^2}{2\omega} \delta(\omega) + \frac{\omega_p^2}{\omega^2} \right] \left(1 - (T/T_c)^2\right) |\Psi(\mathbf{r})|^2 - \frac{\omega_p^2 (T/T_c)^2}{\omega^2 + i\gamma(T)\omega} \\ & - \frac{\Omega_{\text{MIR}}^2}{\omega^2 - \omega_{\text{MIR}}^2 + i\Gamma_{\text{MIR}}\omega} - \sum_{r=1}^{N_{\text{ph}}} \frac{\Omega_{\text{ph}}^2}{\omega^2 - \omega_r^2 + i\gamma_r\omega}. \end{aligned} \tag{22}$$

As explained in Section 2.1, the dielectric function has to be calculated in the rotated frequency space  $i\zeta$  where the details can be found in Ref. [60]. In this scheme, the nanosphere and substrate permittivities are respectively given by  $\epsilon_{\text{ns}}(i\zeta) = \epsilon_{\text{Au}}(i\zeta)$ ,  $\epsilon_{\text{sub}}(i\zeta, \mathbf{r}_\perp, T) = \epsilon_{ab}^{(n)}(i\zeta, \mathbf{r}_\perp, T > T_c)$  and  $\epsilon_{\text{sub}}(i\zeta, \mathbf{r}_\perp, T) = \epsilon_{ab}^{(s)}(i\zeta, \mathbf{r}_\perp, T < T_c)$ .

### 3. Results

We show in Figure 2 the structure of Casimir force at  $T = 2$  K, as a function of the position of the Au nanosphere over the AL. Here, the nanosphere radius  $R = 4$  nm, and  $d = 2R$ . Although the dipole approximation requires, actually,  $d \gg R$ , as mentioned above, in a previous study, it was found that higher multipolar contributions to the force become negligible at this separation [42]. This figure reveals that the Casimir force displays a periodic structure congruent with the spatial charge distribution induced by the AL. It can be observed that the modulation amplitude  $\Delta F = |F_{\max} - F_{\min}|$  is maximized at regions corresponding to the vortex cores, consistently with the finding that the material reflectivity is strongly reduced at these zones. In order to compare how these results are altered with increasing temperature, we present in Figure 3 a cross-section of the Casimir force surface at a fixed value of  $\mathcal{L}_x = 0.5$ , for three different temperatures:  $T = 2$  K,  $T = 40$  K, and  $T = 90$  K, with corresponding lattice size:  $L_x(2 \text{ K}) = 4.1$  nm,  $L_x(40 \text{ K}) = 4.6$  nm, and  $L_x(90 \text{ K}) = 16.4$  nm. We observe that in the low-temperature regime,  $2 \leq T \leq 40$  K, quite similar periodic patterns arise, essentially independent of the temperature, with a relatively small modulation amplitude  $\Delta F \approx 0.04$  pN. On the other hand, for  $T \approx T_c$  the vortex cell size increases, but the force modulation is drastically reduced.

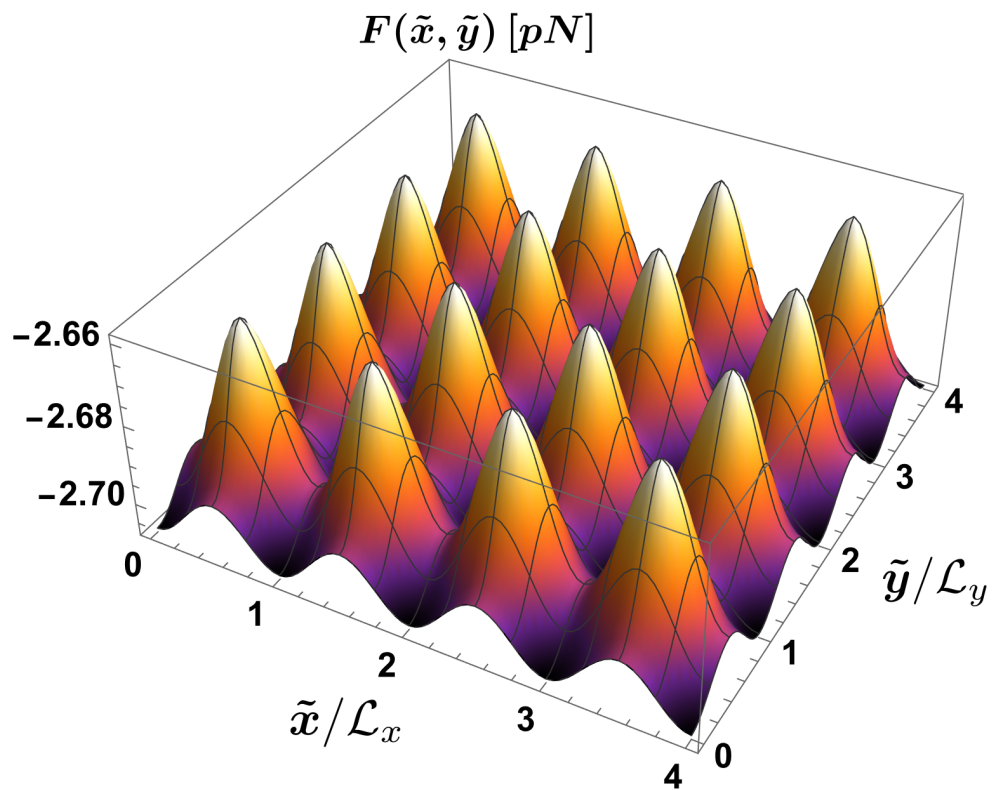


**Figure 2.** Periodic structure of the Casimir force as a function of the location of the Au nanosphere over the Abrikosov lattice at  $T = 2$  K, for a fixed distance  $d = 2R$ . Here,  $R = \mathcal{L}_x(2 \text{ K}) \approx 4$  nm. It can be observed that the minimal strength of the Casimir force corresponds to the vortex cores.

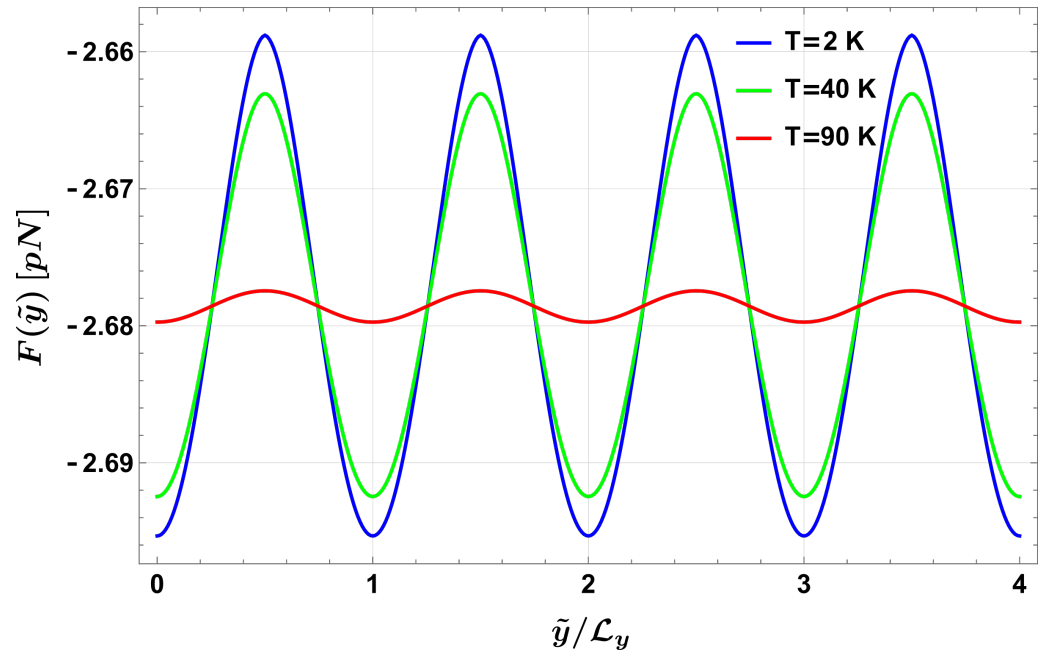


**Figure 3.** Comparison of the Casimir force profiles as a function of the normalized coordinate  $\tilde{y}/\mathcal{L}_y$  along a line passing right above the vortex core ( $\tilde{x}/\mathcal{L}_x = 0.5$ ), and  $d = 2R = 8$  nm, at three different temperatures:  $T = 2$  K,  $T = 40$  K and  $T = 90$  K as indicated. Depending on the temperature, each unit period  $\mathcal{L}_y$  corresponds to spatial periods:  $L_y(2\text{ K}) = 4.1$  nm,  $L_y(40\text{ K}) = 4.6$  nm, and  $L_y(90\text{ K}) = 16.4$  nm. We observe that in the low-temperature regime the force magnitude shows almost coincident values up to  $T = 40$  K, consistent with expectations that vacuum fluctuations ( $\sim \hbar c/d$ ) overwhelm thermal fluctuations ( $\sim k_B T$ ) at nanometer separations. Here,  $\hbar$ ,  $c$ , and  $k_B$  denote the reduced Planck constant, the speed of light, and the Boltzmann constant, respectively.

#### 4. Discussion and Conclusions

The former results have been derived within a mean-field approach that neglects thermal fluctuations of the order parameter and pinning disorder. However, in the weak-interacting limit of Cooper pairs, thermal effects can be taken into account [36]. The effect of disorder in the vortex array can be introduced by adding white noise to the coefficients of the GL free energy and performing the  $\mathcal{Z}$  functional integration, or by performing vortex matter simulations based on the numerical analysis of the time-dependent GL formulation [35,36].

Although the present study was focused on the action of magnetic fields just below the upper critical field,  $H \leq H_{c2}$ , the effect of fields near the lower critical value,  $H \geq H_{c1}$  can be straightforwardly discussed within the clean-limit of the London theory [34]. In that case, the order parameter is given by  $|\phi(r)|^2 \approx (1 + 2\tilde{\xi}_{ab}^2/r^2)^{-1}$ , while the local magnetic induction  $B(r) = \Phi_0 K_0(\sqrt{r^2 + 2\tilde{\xi}_{ab}^2}/\lambda_{ab})/2\pi\lambda_{ab}^2$ , where  $K_0(x)$  is a modified Bessel function. Then, the total order parameter can be built as the product  $\prod_i \phi(|\mathbf{r} - \mathbf{r}_i|)$ , where  $\mathbf{r}_i$  denotes the localization of the different vortices, whereas the total magnetic induction  $\mathbf{B}(\mathbf{r}) = \sum_i \mathbf{B}(|\mathbf{r} - \mathbf{r}_i|)$  [61].

The periodic structure of the system could, actually, induce diffractive effects in the predicted spatial-pattern observed in the Casimir force. Indeed it has been shown how diffraction gratings modify the force [62]. We did not consider this kind of effects because they would occur for wavelengths of the order of the period of the Abrikosov lattice, about 4–16 nm in our case. This corresponds to frequencies higher than 300 eV. For these high values of energy, the dielectric function is constant (tends to the high-frequency value,  $\epsilon_\infty$ ), and no position dependence will be observed.

In conclusion, we presented a general methodology aimed to evaluate the Casimir force in setups constituted by SC materials under the action of an external magnetic field.

We have shown that the Abrikosov vortex lattice displayed by a type II superconductor induces Casimir forces with a periodic structure that mirrors the local charge redistribution due to superconducting currents conducting to magnetic fluxon confinement within the vortex cores. This approach may be applied to SC systems under different conditions of temperature, oxygen doping, and magnetic field configurations, allowing the analysis of alternative orderings competing with vortex matter, such as charge density waves [63], or the investigation of normal matter inside the vortices subject to multiple Andreev reflections [64].

**Author Contributions:** Conceptualization, S. G.C.-L., R.E.-S., G.P. and C.V.; formal analysis, S.G.C.-L., R.E.-S., G.P. and C.V.; methodology, S.G.C.-L., R.E.-S., G.P. and C.V.; software, S.G. C.-L. and C.V.; writing—original draft, S.G. C.-L., R.E.-S., G.P. and C.V.; writing—review and editing, S.G.C.-L., R.E.-S., G.P. and C.V. All authors have read and agreed to the published version of the manuscript.

**Funding:** S.G.C-L acknowledges financial support from UNAM DGAPA PAPIIT Grant No. TA100724. G.P. acknowledges financial support from UNAM DGAPA PAPIIT Grant No. IN104522, UNAM DGAPA PAPIME PE101223 and CONACyT Projects No. 1564464 and No. 1098652. R.E.-S. acknowledges partial support from CONACyT Project No. A1-S-10537.

**Data Availability Statement:** The data presented in this study are available on request from the corresponding author.

**Conflicts of Interest:** The authors declare no conflict of interest.

## References

1. Casimir, H.B.G. On the attraction between two perfectly conducting plates. *Proc. Kon. Ned. Akad. Wet. B* **1948**, *51*, 793–795. Available online: <https://dwc.knaw.nl/DL/publications/PU00018547.pdf> (accessed on 29 January 2024).
2. Lifshitz, E.M. The theory of molecular attractive forces between solids. *Sov. Phys. JETP* **1956**, *2*, 73–83. Available online: <http://jetp.ras.ru/cgi-bin/e/index/e/2/1/p73?a=list> (accessed on 29 January 2024).
3. Lamoreaux, S.K. Demonstration of the Casimir force in the 0.6 to 6  $\mu\text{m}$  range. *Phys. Rev. Lett.* **1997**, *78*, 5–8. [[CrossRef](#)]
4. Harris, B.W.; Chen, F.; Mohideen, U. Precision measurement of the Casimir force using gold surfaces. *Phys. Rev. A* **2000**, *62*, 052109. [[CrossRef](#)]
5. Bressi, G.; Carugno, G.; Onofrio, R.; Ruoso, G. Measurement of the Casimir force between parallel metallic surfaces. *Phys. Rev. Lett.* **2002**, *88*, 041804. [[CrossRef](#)] [[PubMed](#)]
6. Decca, R.S.; López, D.; Fischbach, E.; Krause, D.E. Measurement of the Casimir force between dissimilar metals. *Phys. Rev. Lett.* **2003**, *91*, 050402. [[CrossRef](#)] [[PubMed](#)]
7. Chen, F.; Klimchitskaya, G.L.; Mohideen, U.; Mostepanenko, V.M. Theory confronts experiment in the Casimir force measurements: Quantification of errors and precision. *Phys. Rev. A* **2004**, *69*, 022117. [[CrossRef](#)]
8. Decca, R.S.; López, D.; Fischbach, E.; Klimchitskaya, G.L.; Krause, D.E.; Mostepanenko, V.M. Precise comparison of theory and new experiment for the Casimir force leads to stronger constraints on thermal quantum effects and long-range interactions. *Ann. Phys.* **2005**, *318*, 37–80. [[CrossRef](#)]
9. Krause, D.E.; Decca, R.S.; López, D.; Fischbach, E. Experimental investigation of the Casimir force beyond the proximity-force approximation. *Phys. Rev. Lett.* **2007**, *98*, 050403. [[CrossRef](#)]
10. Jourdan, G.; Lambrecht, A.; Comin, F.; Chevrier, J. Quantitative non-contact dynamic Casimir force measurements. *EPL (Europhys. Lett.)* **2009**, *85*, 31001. [[CrossRef](#)]
11. Chang, C.-C.; Banishev, A.A.; Castillo-Garza, R.; Klimchitskaya, G.L.; Mostepanenko, V.M.; Mohideen, U. Gradient of the Casimir force between Au surfaces of a sphere and a plate measured using an atomic force microscope in a frequency-shift technique. *Phys. Rev. B* **2012**, *85*, 165443. [[CrossRef](#)]
12. Banishev, A.A.; Klimchitskaya, G.L.; Mostepanenko, V.M.; Mohideen, U. Demonstration of the Casimir force between ferromagnetic surfaces of a Ni-coated sphere and a Ni-coated plate. *Phys. Rev. Lett.* **2013**, *110*, 137401. [[CrossRef](#)] [[PubMed](#)]
13. Castillo-Garza, R.; Xu, J.; Klimchitskaya, G.L.; Mostepanenko, V.M.; Mohideen, U. Casimir interaction at liquid nitrogen temperature: Comparison between experiment and theory. *Phys. Rev. B* **2013**, *88*, 075402. [[CrossRef](#)]
14. Klimchitskaya, G.L.; Mohideen, U.; Mostepanenko, V.M. The Casimir force between real materials: Experiment and theory. *Rev. Mod. Phys.* **2009**, *81*, 1827–1885. [[CrossRef](#)]
15. Rodriguez, A.W.; Capasso, F.; Johnson, S.G. The Casimir effect in microstructured geometries. *Nat. Phot.* **2011**, *5*, 211–221. [[CrossRef](#)]
16. Milonni, P.W. *The Quantum Vacuum: An Introduction to Quantum Electrodynamics*; Academic Press, Inc.: San Diego, CA, USA, 2013. [[CrossRef](#)]
17. Milton, K.A. *The Casimir Effect: Physical Manifestations of Zero-Point Energy*; World Scientific Co., Ltd.: Singapore, 2001. [[CrossRef](#)]

18. Bordag, M.; Klimchitskaya, G.L.; Mohideen, U.; Mostepanenko, V.M. *Advances in the Casimir Effect*; Oxford University Press Inc.: New York, NY, USA, 2009. [CrossRef]
19. Sushkov, A.; Kim, W.; Dalvit, D.; Lamoreaux, S. Observation of the thermal Casimir force. *Nat. Phys.* **2011**, *7*, 230–233. [CrossRef]
20. Simpson, W.M.R.; Leonhardt, U. *Forces of the Quantum Vacuum: An Introduction to Casimir Physics*; World Scientific: Singapore, 2015. [CrossRef]
21. Bimonte, G.; López, D.; Decca, R.S. Isoelectronic determination of the thermal Casimir force. *Phys. Rev. B* **2016**, *93*, 184434. [CrossRef]
22. Liu, M.; Xu, J.; Klimchitskaya, G.L.; Mostepanenko, V.M.; Mohideen, U. Precision measurements of the gradient of the Casimir force between ultraclean metallic surfaces at larger separations. *Phys. Rev. A* **2019**, *100*, 052511. [CrossRef]
23. Bimonte, G.; Spreng, B.; Maia Neto, P.A.; Ingold, G.L.; Klimchitskaya, G.L.; Mostepanenko, V.M.; Decca, R.S. Measurement of the Casimir force between 0.2 and 8 mm: Experimental procedures and comparison with theory. *Universe* **2021**, *7*, 93. [CrossRef]
24. Bimonte, G.; Calloni, E.; Esposito, G.; Milano, L.; Rosa, L. Towards measuring variations of Casimir energy by a superconducting cavity. *Phys. Rev. Lett.* **2005**, *94*, 180402. [CrossRef]
25. Bimonte, G.; Born, D.; Calloni, E.; Esposito, G.; Il'ichev, E.; Rosa, L.; Scaldaferrri, O.; Tafuri, F.; Vaglio, R.; Hübner, U. The Aladin2 experiment: Status and perspectives. *J. Phys. A Math. Gen.* **2006**, *39*, 6153–6159. [CrossRef]
26. Bimonte, G.; Calloni, E.; Esposito, G.; Rosa, L. Casimir energy and the superconducting phase transition. *J. Phys. A Math. Gen.* **2006**, *39*, 6161–6171. [CrossRef]
27. Bimonte, G.; Born, D.; Calloni, E.; Esposito, G.; Huebner, U.; Il'ichev, E.; Rosa, L.; Tafuri, F.; Vaglio, R. Low noise cryogenic system for the measurement of the Casimir energy in rigid cavities. *J. Phys. A Math. Theor.* **2008**, *41*, 164023. [CrossRef]
28. Bimonte, G. Casimir effect in a superconducting cavity and the thermal controversy. *Phys. Rev. A* **2008**, *78*, 062101. [CrossRef]
29. Norte, R.A.; Forsch, M.; Wallucks, A.; Marinković, I.; Gröblacher, S. Platform for measurements of the Casimir force between two superconductors. *Phys. Rev. Lett.* **2018**, *121*, 030405. [CrossRef]
30. Bimonte, G. Casimir effect between superconductors. *Phys. Rev. A* **2019**, *99*, 052507. [CrossRef]
31. Villarreal, C.; Caballero-Benitez, S.F. Casimir forces and high- $T_c$  superconductors. *Phys. Rev. A* **2019**, *100*, 042504. [CrossRef]
32. Castillo-López, S.G.; Esquivel-Sirvent, R.; Pirruccio, G.; Villarreal, C. Casimir forces out of thermal equilibrium near a superconducting transition. *Sci. Rep.* **2022**, *12*, 2905. [CrossRef]
33. Abrikosov, A.A. Nobel Lecture: Type-II superconductors and the vortex lattice. *Rev. Mod. Phys.* **2004**, *76*, 975–979. [CrossRef]
34. Annett, J.F. *Superconductivity, Superfluids and Condensates*; Oxford University Press Inc.: New York, NY, USA, 2004. Available online: <https://archive.org/details/superconductivity0000anne/> (accessed on 29 January 2024).
35. Blatter, G.; Feigel'man, M.V.; Geshkenbein, V.B.; Larkin, A.I.; Vinokur, V.M. Vortices in high-temperature superconductors. *Rev. Mod. Phys.* **1994**, *66*, 1125–1388. [CrossRef]
36. Rosenstein, B.; Li, D. Ginzburg-Landau theory of type II superconductors in magnetic field. *Rev. Mod. Phys.* **2010**, *82*, 109–168. [CrossRef]
37. Kwok, W.K.; Welp, U.; Glatz, A.; Koshelev, A.E.; Kihlstrom, K.J.; Crabtree, G.W. Vortices in high-performance high-temperature superconductors. *Rep. Prog. Phys.* **2016**, *79*, 116501. [CrossRef] [PubMed]
38. Suderow, H.; Guillaumon, I.; Rodrigo, J.G.; Vieira, S. Imaging superconducting vortex cores and lattices with a scanning tunneling microscope. *SuST* **2014**, *27*, 063001. [CrossRef]
39. Sonier, J.E.; Brewer, J.H.; Kiefl, R.F.  $\mu$ SR studies of the vortex state in type-II superconductors. *Rev. Mod. Phys.* **2000**, *72*, 769–811. [CrossRef]
40. Scheel, S.; Fermani, R.; Hinds, E. Feasibility of studying vortex noise in two-dimensional superconductors with cold atoms. *Phys. Rev. A* **2007**, *75*, 064901. [CrossRef]
41. Román-Velázquez, C.E.; Noguez, C.; Villarreal, C.; Esquivel-Sirvent, R. Spectral representation of the nonretarded dispersive force between a sphere and a substrate. *Phys. Rev. A* **2004**, *69*, 042109. [CrossRef]
42. Noguez, C.; Román-Velázquez, C.E.; Esquivel-Sirvent, R.; Villarreal, C. High-multipolar effects on the Casimir force: The non-retarded limit. *EPL (Europhys. Lett.)* **2004**, *67*, 191–197. [CrossRef]
43. Noguez, C.; Román-Velázquez, C.E. Dispersive force between dissimilar materials: Geometrical effects. *Phys. Rev. B* **2004**, *70*, 195412. [CrossRef]
44. Neto, P.A.M.; Lambrecht, A.; Reynaud, S. Casimir energy between a plane and a sphere in electromagnetic vacuum. *Phys. Rev. A* **2008**, *78*, 012115. [CrossRef]
45. Canaguier-Durand, A.; Neto, P.A.M.; Caverio-Pelaez, I.; Lambrecht, A.; Reynaud, S. Casimir interaction between plane and spherical metallic surfaces. *Phys. Rev. Lett.* **2009**, *102*, 230404. [CrossRef]
46. Canaguier-Durand, A.; Neto, P.A.M.; Lambrecht, A.; Reynaud, S. Thermal Casimir effect in the plane-sphere geometry. *Phys. Rev. Lett.* **2010**, *104*, 040403. [CrossRef]
47. Bimonte, G. Going beyond PFA: A precise formula for the sphere-plate Casimir force. *EPL (Europhys. Lett.)* **2017**, *118*, 20002. [CrossRef]
48. Tinkham, M. *Introduction to Superconductivity*; Dover Publications, Inc.: Mineola, NY, USA, 2004.
49. Castillo-López, S.; Villarreal, C.; Esquivel-Sirvent, R.; Pirruccio, G. Enhancing near-field radiative heat transfer by means of superconducting thin films. *Int. J. Heat Mass Transf.* **2022**, *182*, 121922. [CrossRef]

50. Nozières, P.; Schmitt-Rink, S. Bose condensation in an attractive fermion gas: From weak to strong coupling superconductivity. *J. Low Temp. Phys.* **1985**, *59*, 195–211. [[CrossRef](#)]
51. Pal, S.; Ganguly, K.; Basu, A.; Sharma, U.D. Gorter-Casimir two fluid model revisited and possible applications to superconductivity. *Int. J. Innov. Res. Phys.* **2019**, *1*, 17–26. [[CrossRef](#)]
52. Landau, L.D.; Lifshitz, E.M. *Statistical Physics*; Elsevier Butterworth-Heinemann: Oxford, UK, 2013. [[CrossRef](#)]
53. Fujita, S.; Godoy, S. *Quantum Statistical Theory of Superconductivity*; Springer Science + Business Media: New York, NY, USA, 1996. [[CrossRef](#)]
54. Lomnitz, M.; Villarreal, C.; de Llano, M. BEC model of high- $T_c$  superconductivity in layered cuprates. *Int. J. Mod. Phys. B* **2013**, *27*, 1347001. [[CrossRef](#)]
55. Zuev, Y.; Kim, M.S.; Lemberger, T.R. Correlation between superfluid density and  $T_c$  of underdoped  $\text{YBa}_2\text{Cu}_3\text{O}_{6+x}$  near the superconductor-insulator transition. *Phys. Rev. Lett.* **2005**, *95*, 137002. [[CrossRef](#)] [[PubMed](#)]
56. Chen, Q.; Stajic, J.; Tan, S.; Levin, K. BCS–BEC crossover: From high temperature superconductors to ultracold superfluids. *Phys. Rep.* **2005**, *412*, 1–88. [[CrossRef](#)]
57. Bonn, D.A.; O’Reilly, A.H.; Greedan, J.E.; Stager, C.V.; Timusk, T.; Kamarás, K.; Tanner, D.B. Far-infrared properties of ab-plane oriented  $\text{YBa}_2\text{Cu}_3\text{O}_{7-\delta}$ . *Phys. Rev. B* **1988**, *37*, 1574–1579. [[CrossRef](#)] [[PubMed](#)]
58. Timusk, T.; Herr, S.L.; Kamarás, K.; Porter, C.D.; Tanner, D.B.; Bonn, D.A.; Garrett, J.D.; Stager, C.V.; Greedan, J.E.; Reedyk, M. Infrared studies of ab-plane oriented oxide superconductors. *Phys. Rev. B* **1988**, *38*, 6683–6688. [[CrossRef](#)] [[PubMed](#)]
59. Basov, D.N.; Timusk, T. Electrodynamics of high- $T_c$  superconductors. *Rev. Mod. Phys.* **2005**, *77*, 721–779. [[CrossRef](#)]
60. Klimchitskaya, G.L.; Mohideen, U.; Mostepanenko, V.M. Kramers–Kronig relations for plasma-like permittivities and the Casimir force. *J. Phys. A Math. Theor.* **2007**, *40*, F339–F346. [[CrossRef](#)]
61. Brandt, E.H. The flux-line lattice in superconductors. *Rep. Prog. Phys.* **1995**, *58*, 1465–1594. [[CrossRef](#)]
62. Intravaia, F.; Koev, S.; Jung, I.W.; Talin, A.A.; Davids, P.S.; Decca, R.S.; Aksyuk, V.A.; Dalvit, D.A.; López, D. Strong Casimir force reduction through metallic surface nanostructuring. *Nat. Commun.* **2013**, *4*, 2515. [[CrossRef](#)]
63. Chang, J.; Blackburn, E.; Holmes, A.T.; Christensen, N.B.; Larsen, J.; Mesot, J.; Liang, R.; Bonn, D.A.; Hardy, W.N.; Watenphul, A.; et al. Direct observation of competition between superconductivity and charge density wave order in  $\text{YBa}_2\text{Cu}_3\text{O}_{6.67}$ . *Nat. Phys.* **2012**, *8*, 871–876. [[CrossRef](#)]
64. Huebener, R.P. The Abrikosov vortex lattice: Its discovery and impact. *J. Supercond. Nov. Magn.* **2019**, *32*, 475–481. [[CrossRef](#)]

**Disclaimer/Publisher’s Note:** The statements, opinions and data contained in all publications are solely those of the individual author(s) and contributor(s) and not of MDPI and/or the editor(s). MDPI and/or the editor(s) disclaim responsibility for any injury to people or property resulting from any ideas, methods, instructions or products referred to in the content.